Talanta 225 (2021) 122046

Contents lists available at ScienceDirect

Talanta

journal homepage: www.elsevier.com/locate/talanta

Enhancing near-infrared AIE of photosensitizer with twisted intramolecular charge transfer characteristics via rotor effect for AIE imaging-guided photodynamic ablation of cancer cells

Dong-Hui Wang [a,b], Li-Jian Chen [b], Xu Zhao [b], Xiu-Ping Yan [a,b,*]

[a] Key Laboratory of Synthetic and Biological Colloids, Ministry of Education, School of Chemical and Material Engineering, Jiangnan University, Wuxi, 214122, China
[b] Institute of Analytical Food Safety, School of Food Science and Technology, Jiangnan University, Wuxi, 214122, China

ARTICLE INFO

Keywords:
Near-infrared aggregation-induced emission
Imaging
Photodynamic therapy
Photosensitizer
Twisted intramolecular charge transfer

ABSTRACT

Near-infrared (NIR) aggregation-induced emission (AIE) of previous organic photosensitizers is usually weak because of the competition between twisted intramolecular charge transfer (TICT) effect and AIE. Herein, we report a rational molecular design strategy to boost NIR AIE of photosensitizers and still to keep strong $^1O_2$ production capacity via rotor effect. To this end, one new triphenylamine (TPA)-based AIE photosensitizer, TPAM-1, is designed to give strong ability to generate $^1O_2$ but weak NIR fluorescence in the aggregate state due to the strong TICT effect. Another new TPA-based AIE photosensitizer, TPAM-2, is designed by introducing three *p*-methoxyphenyl units as rotors into the structure of TPAM-1 to modulate the competition between AIE and TICT. TPAM-1 and TPAM-2 exhibit stronger ability to generate $^1O_2$ in the aggregate state than the commercial photosensitizer, Ce6. Furthermore, TPAM-2 gives much brighter NIR luminescence (25-times higher quantum yield) than TPAM-1 in the aggregate state due to the rotor effect. TPAM-2 with strong NIR AIE and $^1O_2$ production capability was encapsulated by DSPE-PEG_{2000} to give good biocompatibility. The DSPE-PEG_{2000}-encapsulated TPAM-2 nanoparticles show good cell imaging performance and remarkable photosensitive activity for killing HeLa cells. This work provides a new way for designing ideal photosensitizers for AIE imaging-guided photodynamic therapy.

1. Introduction

Photodynamic therapy (PDT) is an alternative therapeutic modality for skin malignancies and other organ cancers such as lung and bladder tumors [1–6]. In PDT, a photosensitizer being irradiated by a definite light source is needed for the production of singlet oxygen ($^1O_2$) to inhibit the growth of cancer cells and finally cause tumor necrosis [7–11]. PDT is recognized as a more appropriate method to cure cancers than traditional treatment methods such as surgery, chemotherapy and radiation therapy owing to its noninvasiveness, hypotoxicity and improvement of the quality of life for patients [12]. Imaging-guided PDT is necessary for precise and effective treatment [13]. Bright near-infrared (NIR) fluorescence, strong ability to generate $^1O_2$ as well as good biocompatibility are significant for a photosensitizer in the application of imaging-guided PDT. However, traditional NIR fluorescent photosensitizers such as BODIPY derivatives and porphyrin derivatives can easily form π-π aggregates in the physiological environment [14,15], which may quench fluorescence, reduce $^1O_2$ production and impair the performance of imaging-guided PDT.

Recently, aggregation-induced emission (AIE) has received great interest in diverse areas [16–21], especially in the field of bioprobes for fluorescence imaging and cancer therapy [22–28]. Compared to traditional photosensitizers, photosensitizers with AIE characteristics are more suitable for imaging-guided PDT because they exhibit stronger fluorescence along with the ability to generate reactive oxygen species (ROS) in the aggregate state than in the discrete molecular state [29–32]. However, AIE molecules always have twisted structures based on the restriction of intramolecular rotation (RIR) mechanism [33], and most of AIE photosensitizers exhibit short-wavelength absorption (≤550 nm) and fluorescence (≤650 nm), reducing the performance of imaging-guided PDT because of low penetration depth and autofluorescence interference from bio-tissues. To overcome this

* Corresponding author. Key Laboratory of Synthetic and Biological Colloids, Ministry of Education, School of Chemical and Material Engineering, Jiangnan University, Wuxi, 214122, China.
E-mail address: xpyan@jiangnan.edu.cn (X.-P. Yan).

https://doi.org/10.1016/j.talanta.2020.122046
Received 17 November 2020; Received in revised form 17 December 2020; Accepted 21 December 2020
Available online 24 December 2020

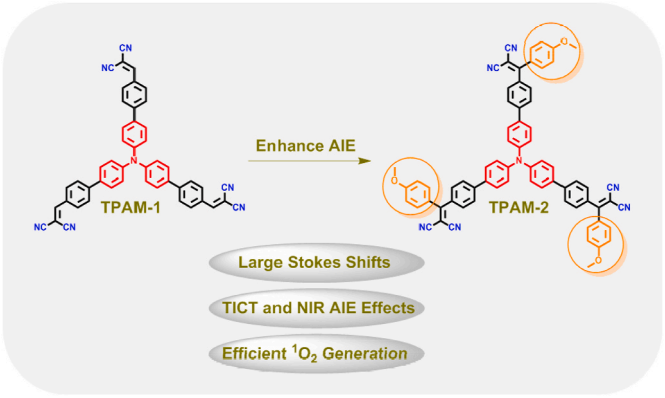

Fig. 1. Illustration for the molecular design, chemical structures and characteristics of **TPAM-1** and **TPAM-2**.

shortcoming, one of the popular strategies is to construct a donor-acceptor (D-A) system in one small organic fluorophore [34]. This strategy enables the red-shift of the absorption and emission of the fluorophore, but with the loss of fluorescence in aqueous media due to the powerful twisted intramolecular charge transfer (TICT) characteristic [35,36]. Furthermore, the fluorophore with a D-A system can facilitate the separation of the highest occupied molecular orbital (HOMO) and the lowest unoccupied molecular orbital (LUMO) distribution to improve the probability of intersystem crossing (ISC) process, so that the ROS generation ability of the fluorophore can be improved [10,37]. Obviously, there is a competition between AIE and TICT. Recently, several effective physical methods have been reported to tune the competition between molecular luminescence and ROS production [29,38]. However, it is still a challenge to rationally modulate the competition between AIE and TICT of a photosensitizer in aqueous media through facile molecular design, which finally determines the quality of imaging and PDT.

Here, we report a rational molecular design strategy to boost NIR AIE of photosensitizers with good $^1O_2$ production capacity via rotor effect for imaging-guided PDT. As a proof of concept (Fig. 1), one new triphenylamine (TPA)-based AIE photosensitizer **TPAM-1** is designed to possess a rotatable D–π bridge–A (D–π–A) configuration to achieve HOMO-LUMO separation and strong TICT effect for effective $^1O_2$ generation and weak NIR fluorescence in the aggregate state. Another new AIE photosensitizer **TPAM-2** is designed by introducing three *p*-methoxyphenyl units as rotors with certain rigidity and electron-donating properties into the molecular skeleton of **TPAM-1** to modulate the competition between AIE and TICT for bright NIR fluorescence along with good $^1O_2$ generation ability in the aggregate state. As a result, the prepared **TPAM-2** not only gives 25 times higher fluorescence quantum yield than **TPAM-1** in the aggregate state, but also exhibits better $^1O_2$ generation ability than the most used photosensitizer, Ce6. 1,2-distearoyl-sn-glycero-3-phosphoethanolamine-*N*-[methoxy(polyethylene glycol)-2000] (DSPE-PEG_{2000})-encapsulated **TPAM-2** nanoparticles are further fabricated to improve their water dispersibility and biocompatibility for successful imaging-guided photodynamic ablation of cancer cells. This work provides a new way for designing ideal photosensitizers for AIE imaging-guided PDT.

2. Experimental section

Synthesis of TPAM-1: A mixture of compound **1** (0.10 g, 0.18 mmol), malonitrile (0.053 g, 0.81 mmol), and ammonium acetate (0.0040 g, 0.054 mmol) was reacted in a solution (glacial acetic acid: 1 mL, pyridine: 5 mL) at room temperature for 24 h. Then, water was added to the above mixture to get the red solid. The solid was filtered off, washed with water for several times, and purified by column chromatography with DCM/petroleum ether (10/1, v/v) as the eluent to obtain **TPAM-1** as a red powder (0.085 g, 68%). ^{1}H NMR (400 MHz, $CDCl_3$, ppm): δ 8.00 (d, J = 8.4 Hz, 6H, Ar*H*), 7.78 (s, 3H, C*H*), 7.77 (d, J = 8.8 Hz, 6H, Ar*H*), 7.62 (d, J = 8.4 Hz, 6H, Ar*H*), 7.29 (d, J = 8.8 Hz, 6H, Ar*H*). ^{13}C NMR (100 MHz, $CDCl_3$, ppm): δ 159.0, 147.7, 146.4, 133.9, 131.6, 129.6, 128.4, 127.4, 124.8, 114.0, 112.9, 81.7. ESI-MS, m/z: [M] $^+$ calcd 701.2, found 701.1.

Synthesis of Compound 3: Compound **2** (0.87 g, 3.00 mmol), bis(pinacolato)diborane (1.53 g, 6.019 mmol), potassium acetate (0.98 g, 10.00 mmol), Pd(dppf)Cl_2 (0.11 g, dppf = 1,1′-bis (diphenylphosphanyl) ferrocene) and dioxane (15 mL) were mixed in a Schlenk tube, and carefully frozen with liquid N_2 and degassed by pump. The above mixture was reacted at 85 °C for 2 days. Then, the solvent was removed in a rotary evaporator to gain the black residue. DCM was used to extract the crude product from aqueous solution of the above residue. The DCM solution of the crude product was collected and dried over $MgSO_4$. After removing the solvent, the crude product was further purified by column chromatography using petroleum ether/ethyl acetate (10/1, v/v) as the eluent to acquire a white solid **3** (0.80 g, 79%). ^{1}H NMR (400 MHz, $CDCl_3$, ppm): δ 7.91 (d, J = 8.4 Hz, 2H, Ar*H*), 7.82 (d, J = 9.2 Hz, 2H, Ar*H*), 7.72 (d, J = 8.4 Hz, 2H, Ar*H*), 6.96 (d, J = 9.2 Hz, 2H, Ar*H*), 3.89 (s, 3H, OCH_3), 1.37 (s, 12H, CH_3). ^{13}C NMR (100 MHz, $CDCl_3$, ppm): δ 195.7, 163.4, 140.6, 134.6, 132.6, 130.1, 128.8, 113.6, 84.2, 55.5, 25.0. ESI-MS, m/z: [M] $^+$ calcd 338.2, found 338.2.

Synthesis of Compound 4: A mixture of tris(4-bromophenyl)amine (0.40 g, 0.84 mmol), compound **3** (1.02 g, 3.016 mmol), K_2CO_3 (3.50 g, 25.38 mmol), THF/H_2O (9 mL/3 mL), and Pd(PPh_3)$_4$ (0.087 g, 3%) in a Schlenk tube was carefully frozen with liquid N_2 and degassed by pump. The above mixture was reacted at 60 °C for 18 h. DCM was employed to extract the crude product from aqueous solution. The DCM solution was collected and dried over $MgSO_4$. After removing DCM, the crude product was purified by column chromatography with DCM/ethyl acetate (50/1, v/v) as the eluent to gain a chartreuse solid **4** (0.60 g, 82%). ^{1}H NMR (400 MHz, $CDCl_3$, ppm): δ 7.88 (d, J = 5.6 Hz, 6H, Ar*H*), 7.85 (d, J = 4.8 Hz, 6H, Ar*H*), 7.71 (d, J = 8.4 Hz, 6H, Ar*H*), 7.62 (d, J = 8.4 Hz, 6H, Ar*H*), 7.30 (d, J = 8.8 Hz, 6H, Ar*H*), 6.99 (d, J = 9.2 Hz, 6H, Ar*H*), 3.91 (s, 9H, OCH_3). ^{13}C NMR (100 MHz, $CDCl_3$, ppm): δ 195.2, 163.3, 147.4, 144.1, 136.8, 134.9, 132.6, 130.7, 130.5, 128.4, 126.5, 124.8, 113.7, 55.7. ESI-MS, m/z: [M] $^+$ calcd 875.3, found 875.3.

Synthesis of TPAM-2: compound **4** (0.20 g, 0.23 mmol) and malononitrile (0.30 g, 4.60 mmol) were dissolved in DCM (30 mL) in a flask. Then, titanium tetrachloride (0.5 mL, 4.60 mmol) was slowly added to the above mixture at 0 °C. After the mixture was stirred for 0.5 h, pyridine (0.4 mL, 4.60 mmol) was added and stirred for another 0.5 h. Then, the above mixture was reacted at 40 °C for 24 h. The DCM solution of the crude product was washed with water for several times. The above DCM solution was collected and dried over $MgSO_4$. After removing DCM, the residue was further purified by column chromatography (silica, DCM/ethyl acetate = 100/1, v/v). The product **TPAM-2** was a red solid (0.21 g, 90%). ^{1}H NMR (400 MHz, $CDCl_3$, ppm): δ 7.70 (d, J = 8.8 Hz, 6H, Ar*H*), 7.60 (d, J = 8.8 Hz, 6H, Ar*H*), 7.51 (d, J = 8.8 Hz, 6H, Ar*H*), 7.48 (d, J = 9.2 Hz, 6H, Ar*H*), 7.28 (d, J = 8.8 Hz, 6H, Ar*H*), 6.99 (d, J = 8.8 Hz, 6H, Ar*H*), 3.90 (s, 9H, OCH_3). ^{13}C NMR (100 MHz, $CDCl_3$, ppm): δ 173.9, 163.7, 147.6, 144.7, 134.9, 134.3, 133.2, 131.5, 128.4, 128.3, 126.9, 124.8, 114.9, 114.8, 114.4, 78.5, 55.8. ESI-MS, m/z: [M] $^+$ calcd 1019.4, found 1019.4.

Preparation of TPAM-2 NPs: **TPAM-2** NPs were synthesized via a nanoprecipitation approach [39]. A THF solution (1 mL) containing **TPAM-2** (1 mg) and DSPE-PEG_{2000} (2 mg) was quickly injected into water (9 mL), and sonicated for 5 min in a ultrasonic homogenizer. The above mixture was vigorously stirred overnight in a fume cupboard to remove THF and filtered using a 0.22 μm syringe filter to obtain the final **TPAM-2** NPs.

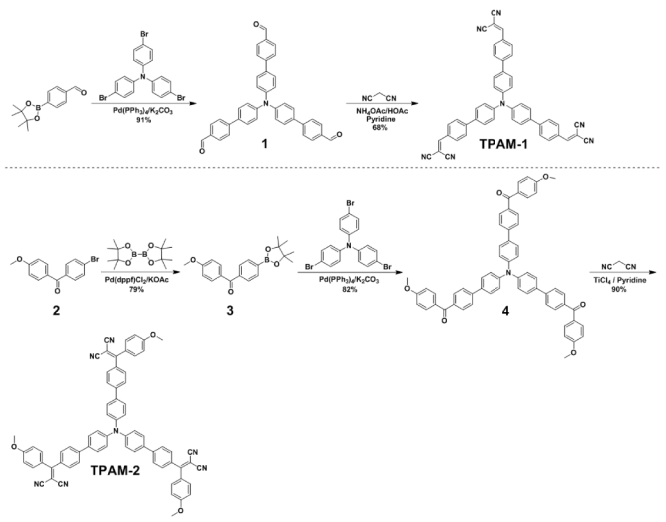

Scheme 1. Synthetic routes for **TPAM-1** and **TPAM-2**.

3. Results and discussion

Fig. 1 shows the molecular design, chemical structure and characteristics of **TPAM-1** and **TPAM-2**. **TPAM-1** was designed to possess twisted D–π–A configuration with a triphenylamine segment as strong electron donor, a benzene ring as the π bridge and a dicyano segment as strong electron accepter, so that **TPAM-1** exhibits good $^1O_2$ generation but weak or even no NIR fluorescence in aqueous media due to strong TICT effect. The D–π–A system in photosensitizers can facilitate the separation of HOMO and LUMO distribution, which favors singlet–triplet energy gap (ΔE_{ST}) reduction and finally ISC process [10]. Such photosensitizers with D–π–A system, therefore, can improve the photosensitization process and give long-wavelength absorbance and emission.

To modulate the competition between AIE and TICT, **TPAM-2** was designed to have three more molecular rotors by introducing *p*-methoxyphenyl groups into the structure of **TPAM-1** to improve the NIR AIE through decreasing intermolecular interactions due to rotor effect. Meanwhile, the *p*-methoxyphenyl group can serve as electron donor to disturb the TICT effect through balancing charge transfer between the triphenylamine and the dicyano segments. Time-dependent density functional theory (TD-DFT) calculation shows that both **TPAM-1** and **TPAM-2** have favorable HOMO-LUMO separation and small ΔE_{ST} (0.22 eV for **TPAM-1** and 0.17 eV for **TPAM-2**) (Fig. S1).

TPAM-1 and **TPAM-2** were synthesized via classical reactions such as the Suzuki–Miyaura coupling reaction and the condensation reaction with the total yield of 62% and 51%, respectively (Scheme 1). Their structures were identified by ^{1}H NMR, ^{13}C NMR and ESI-MS spectroscopy (Fig. S2-S15).

The optical properties of **TPAM-1** and **TPAM-2** were firstly investigated. Different solvents with various polarities, including toluene, dioxane, chloroform, tetrahydrofuran (THF), dichloromethane (DCM), acetone, acetonitrile and dimethyl sulfoxide (DMSO) were used to examine solvatochromic effect. Solvent polarity had a little effect on the absorption spectra of the two fluorophores (Fig. S16-S17), but exhibited a significant influence on their fluorescence spectra. **TPAM-1** exhibited strong green fluorescence in non-polar solvent toluene. Increase of the solvent polarity from toluene to DMSO led to a gradual decrease of fluorescence intensity in conjunction with a bathochromic shift to NIR region (Fig. 2a,c). **TPAM-2** also possessed a similar bathochromic shift of the fluorescence spectrum as the solvent polarity increased (Fig. 2b, d). These results show that **TPAM-1** and **TPAM-2** have TICT characteristic due to their rotatable D–π–A structures.

DMSO/water mixture was used as a solvent system to further investigate the TICT and AIE properties of the two fluorophores. DMSO and water were selected because their strong polarity is beneficial for revealing the TICT characteristic [40]. In addition, DMSO and water are good solvent and poor solvent for the two fluorophores, respectively. The AIE characteristic of a fluorophore is usually investigated in a mixed solvent system which contains a good solvent and a poor solvent to modulate the molecular aggregation. **TPAM-1** and **TPAM-2** in DMSO/-water should exhibit almost no fluorescence because of the strong TICT effect in a strong polar solvent system. In fact, both fluorophores gave almost no fluorescence only when the water fraction (f_w) in DMSO/-water was less than 20%, then showed increasing fluorescence intensity with f_w in the range of 30%–90%. In such a water-containing binary solvent system, there is a competition between TICT and AIE effect on

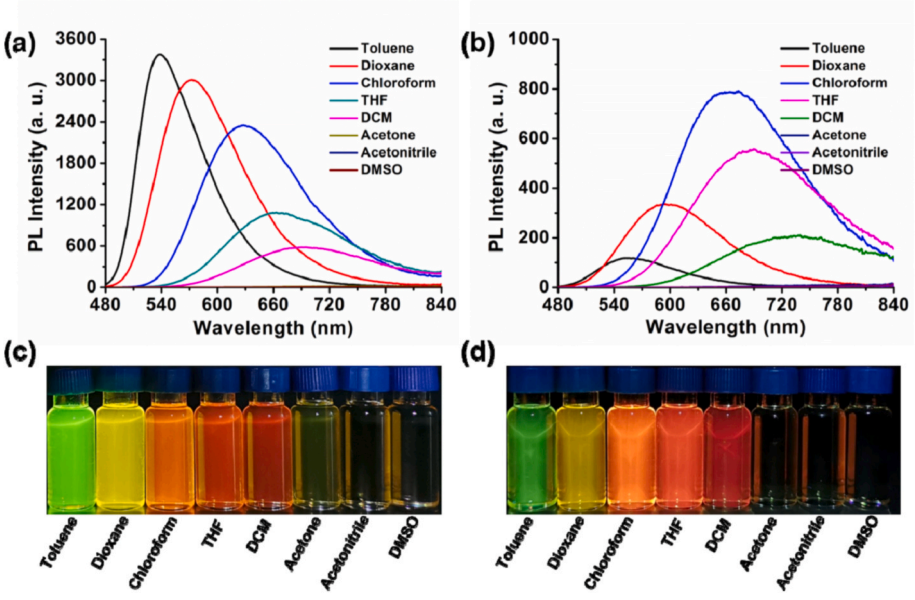

Fig. 2. Effect of solvent on the photoluminescence (PL) of **TPAM-1** and **TPAM-2** (10 μM): (a) PL spectra of **TPAM-1**; (b) PL spectra of **TPAM-2**; (c) PL images of **TPAM-1**; (d) PL images of **TPAM-2**. The PL spectra were collected under excitation at 450 nm for **TPAM-1** and 428 nm for **TPAM-2**, while the PL images were collected under UV irradiation at 365 nm.

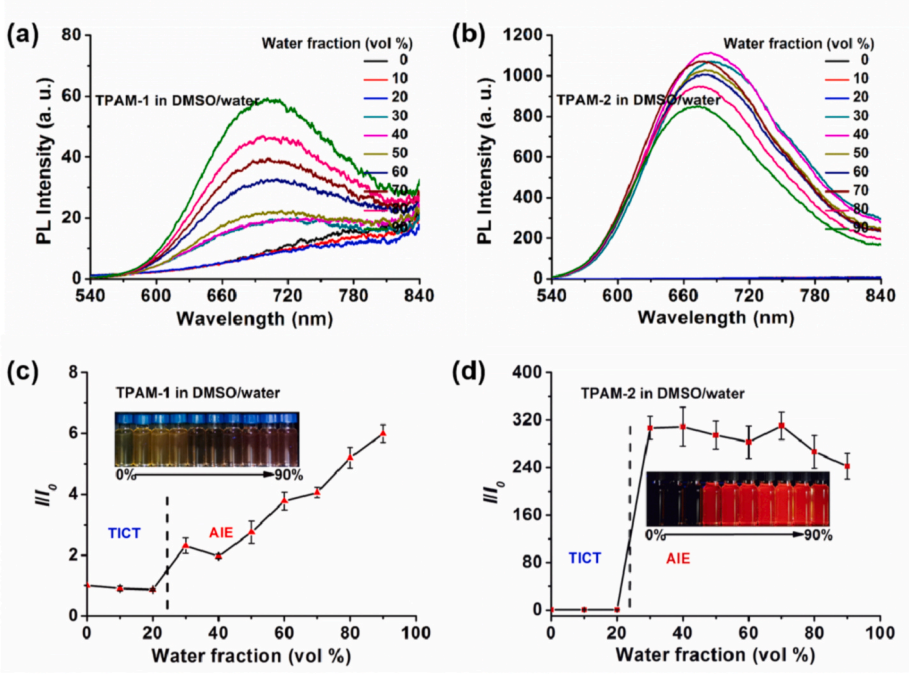

Fig. 3. PL spectra: (a) **TPAM-1** in DMSO/water; (b) **TPAM-2** in DMSO/water. Plots of the relative PL intensity (I/I_0) against water fraction in DMSO/water: (c) **TPAM-1**; (d) **TPAM-2**. I_0 denotes the PL intensity of **TPAM-1** or **TPAM-2** in pure DMSO. Insets: the PL photos of **TPAM-1** or **TPAM-2** in DMSO/water with different water fractions under 365 nm UV irradiation. [**TPAM-1**] = [**TPAM-2**] = 10 μM.

the fluorescence of the fluorophores with rotatable D–π–A structures. The above results indicate that TICT effect was dominating when f_w < 20%, while AIE effect was prevailing when f_w > 30% due to the poor water solubility of the fluorophores. In addition, the maximum emission of the fluorophores showed a blue shift when f_w > 30% due to the decrease of the internal polarity of the fluorophores. In the aggregate state (f_w = 90%), **TPAM-1** and **TPAM-2** possessed the maximum fluorescence at 702 nm and 674 nm, respectively. However, **TPAM-1** showed very weak fluorescence while **TPAM-2** exhibited strong fluorescence (Fig. 3a–d). **TPAM-2** possessed 25 times higher fluorescence quantum yield than **TPAM-1** in the aggregate state (0.40% for **TPAM-1** and 10% for **TPAM-2**). The quantum yield data were calculated based on a commercial dye Rhodamine B in a relative manner. These results indicate that the three more rotors in **TPAM-2** effectively decreased intermolecular interactions in the aggregate state due to the increased torsion of the structure, which in turn reduced the energy decay via non-radiative pathways. The electron-donating rotors of **TPAM-2** could also disturb the TICT effect through balancing the D–π–A strength [40]. Therefore, the competition of AIE over TICT was effectively enhanced through modulating molecular rotors.

The attractive optical properties of **TPAM-1** and **TPAM-2** prompted us to investigate the PDT potential of the two fluorophores. **TPAM-1** and **TPAM-2** containing a D–π–A structure can reduce ΔE_{ST} and favor the ISC process, making them promising as photosensitizers. Therefore, the ability of **TPAM-1** and **TPAM-2** for generating $^1O_2$ was evaluated with 9,10-anthracenediyl-bis(methylene) dimalonic acid (ABDA) as an indicator. The generated $^1O_2$ enables effective reduction of the absorbance of ABDA due to redox reaction. DMSO was selected as a good solvent to investigate the ability of two fluorophores for generating $^1O_2$ in the discrete molecular state. Upon white light irradiation (400–700 nm, 4 mW cm^{-2}) for 8 min, the absorbance of ABDA showed no change in the presence of **TPAM-1** or **TPAM-2** in DMSO (Fig. 4a and b). Showing both **TPAM-1** and **TPAM-2** in the discrete molecular state had no ability for $^1O_2$ generation due to the fast energy decay from the powerful intramolecular rotation via non-radiative pathways [10].

DMSO/water (1:99, v/v) was selected as a poor solvent system to further study the ability of the two fluorophores for generating $^1O_2$ in the aggregate state. ABDA, **TPAM-1** or **TPAM-2** were quite stable in DMSO/water (1:99, v/v) due to no change of their absorption spectra under light irradiation (400–700 nm, 4 mW cm^{-2}) for 8 min (Fig. S19). However, the absorbance of ABDA significantly decreased in the presence of **TPAM-1** or **TPAM-2** under the same irradiation condition (Fig. 4c–f), indicating the generation of $^1O_2$ in the aggregate state of **TPAM-1** or **TPAM-2**. In contrast, only small decrease of the absorbance of ABDA in the presence of a commercial photosensitizer, Ce6 (Fig. 4e). These results show much stronger $^1O_2$ generation ability of **TPAM-1** or **TPAM-2** than Ce6 in the aggregate state. In addition, **TPAM-1** made ABDA degrade much faster than **TPAM-2**. 59% and 33% of ABDA were oxidized in 1 min by the $^1O_2$ generated from **TPAM-1** and **TPAM-2**, respectively. Moreover, **TPAM-1** and **TPAM-2** showed good aggregation-improved ability for generating $^1O_2$ because the restriction of intramolecular rotation in their aggregate states could effectively reduce energy decay via non-radiative pathways. Although **TPAM-2** showed a little weaker $^1O_2$ generation ability than **TPAM-1** in the aggregate state after introducing three more rotors, **TPAM-2** gave strong NIR AIE fluorescence. Considering both the fluorescence property and the $^1O_2$ generation ability, **TPAM-2** should be promising for imaging-guided PDT.

The potential of **TPAM-2** for imaging-guided PDT was further studied due to the good NIR AIE fluorescence and $^1O_2$ generation ability of **TPAM-2**. The hydrophobic **TPAM-2** is not suitable for direct application in the physiological environment, so amphiphilic polymer DSPE-PEG$_{2000}$ was employed to encapsulate **TPAM-2** for the preparation of hydrophilic and biocompatible **TPAM-2** nanoparticles for further biological study. Amphiphilic polymer encapsulated nanoparticles have been widely applied in the field of biology and medicine [41–44]. The DSPE-PEG$_{2000}$ encapsulated **TPAM-2** nanoparticles (**TPAM-2** NPs) were fabricated by a nanoprecipitation method (Fig. 5a). The transmission electron microscopy (TEM) image reveals that the as-prepared **TPAM-2** NPs had spherical morphology (Fig. S20). Dynamic light scattering (DLS) results show that the as-prepared **TPAM-2** NPs had the hydrodynamic diameter of 45 ± 5 nm. In addition, the as-prepared **TPAM-2**

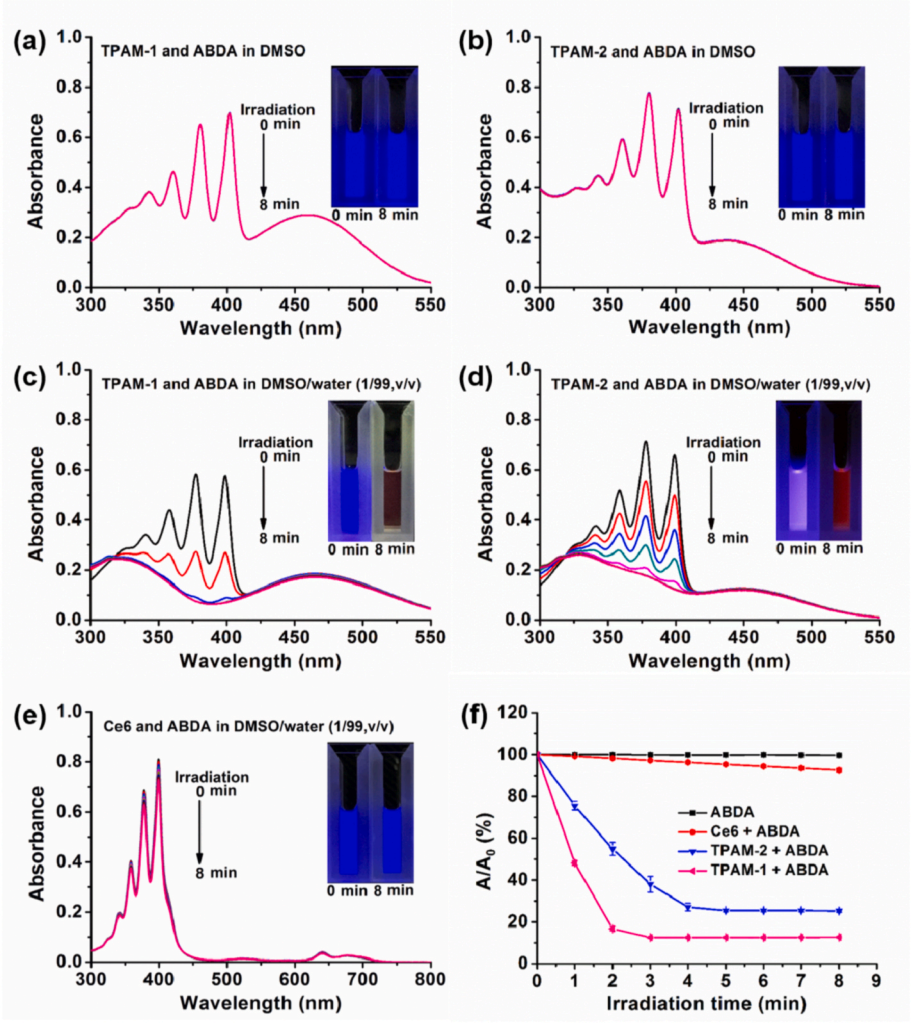

Fig. 4. UV–vis spectra of ABDA in the presence of different photosensitizers under white light irradiation (4 mW cm^{-2}) in different solvent systems: (a) **TPAM-1** in DMSO; (b) **TPAM-2** in DMSO; (c) **TPAM-1** in DMSO/water (1/99, v/v); (d) **TPAM-2** in DMSO/water (1/99, v/v); (e) Ce6 in DMSO/water (1/99, v/v). (f) Time-dependent absorbance of ABDA in the presence of different photosensitizers under white light irradiation in DMSO/water (1/99, v/v), where A_0 and A are the absorbances of ABDA at 378 nm before and after irradiation, respectively. Insets: the fluorescent photos of ABDA in the presence of fluorophores before (0 min) and after (8 min) white light irradiation under 365 nm UV irradiation. [ABDA] = 50 μM; [**TPAM-1**] = [**TPAM-2**] = [Ce6] = 5 μM.

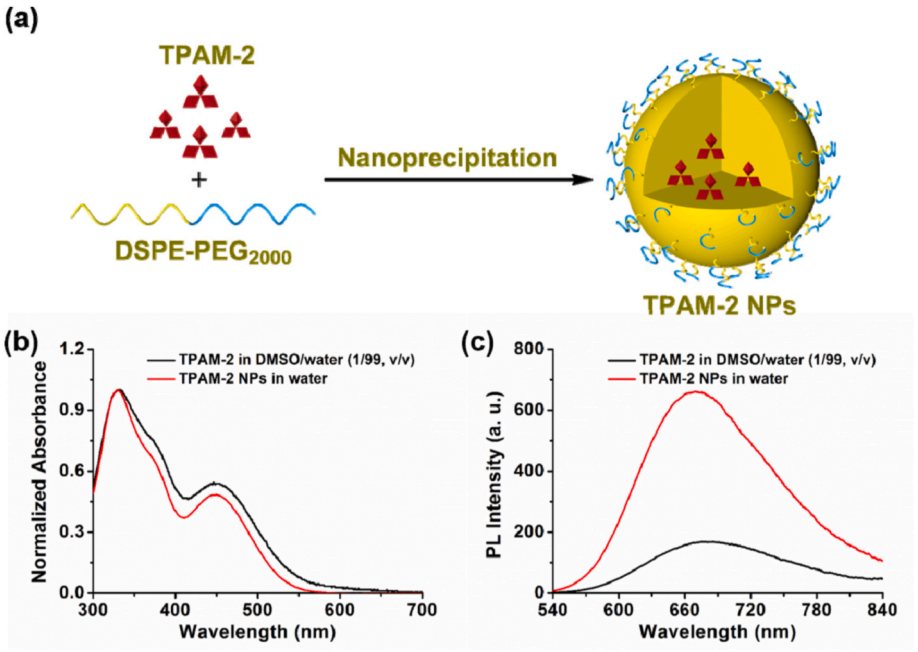

Fig. 5. (a) Schematic illustration for preparing **TPAM-2** NPs. (b) UV–vis spectra of **TPAM-2** in DMSO/water (1/99, v/v) and **TPAM-2** NPs in water. (c) PL spectra of **TPAM-2** in DMSO/water (1/99, v/v) and **TPAM-2** NPs in water (λ_{ex} = 450 nm). [**TPAM-2**] = 5 μM.

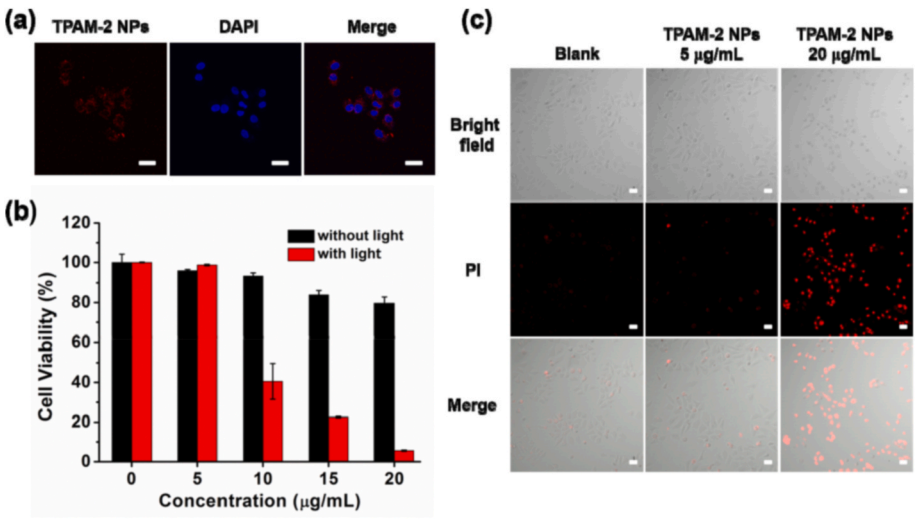

Fig. 6. (a) Cell images in the presence of **TPAM-2** NPs (the blue fluorescence came from 4′,6-diamidino-2-phenylindole (DAPI) stained cell nuclei), Scale bar: 30 μm; (b) Cell viability of **TPAM-2** NPs treated HeLa cells under white light irradiation (130 mW cm^{-2}, 30 min) or in the dark. (c) Cell apoptosis imaging of **TPAM-2** NPs treated HeLa cells under white light irradiation (130 mW cm^{-2}) for 30 min. Dead cells were stained by PI (100 μg mL^{-1}) for 10 min. Scale bar: 30 μm. (For interpretation of the references to colour in this figure legend, the reader is referred to the Web version of this article.)

NPs showed good stability in water due to no obvious change in their diameters for half a month (Fig. S21).

Both **TPAM-2** aggregates in DMSO/water (1:99, v/v) and **TPAM-2** NPs in water exhibited similar features of the UV–vis absorption spectra with two peaks at 330 and 450 nm (Fig. 5b), and the NIR fluorescence spectra with the maximum fluorescence at 670 nm along with large Stokes shift (220 nm) (Fig. 5c). However, the **TPAM-2** NPs in water gave 3.9 times higher fluorescence intensity than **TPAM-2** aggregates in DMSO/water (1/99, v/v). The fluorescence quantum yield of the **TPAM-2** NPs is 14%, which is 1.4 times higher than the **TPAM-2** aggregates (10%). The results suggest that the formation of nanoparticles could weaken the interaction of molecules with the polar environment to further restrain the TICT effect and improve the AIE effect. However, the **TPAM-2** NPs exhibited no better capability for generating $^1O_2$ than **TPAM-2** aggregates in DMSO/water (1/99, v/v) because the further enhancement of the fluorescence can reduce $^1O_2$ production (Fig. S22-S23) [29]. Even so, the **TPAM-2** NPs still had good ability to generate $^1O_2$ for imaging-guided PDT application.

We then further demonstrate the potential of **TPAM-2** NPs for fluorescence imaging-guided photodynamic ablation of cancer cells. HeLa cells were used as a model for this purpose. **TPAM-2** NPs were incubated with HeLa cells for 12 h to obtain fluorescence images on laser confocal fluorescence microscopy. The results show that **TPAM-2** NPs could effectively stain the cytoplasm with red fluorescence, indicating good fluorescence imaging performance of **TPAM-2** NPs (Fig. 6a). The PDT performance of **TPAM-2** NPs towards HeLa cells was evaluated by a 3-(4,5-dimethylthiazol-2-yl)-2,5-diphenyltetrazolium bromide (MTT) method. There was still about 80% of cell viability in the presence of **TPAM-2** NPs (20 μg mL^{-1}) without white light irradiation (Fig. 6b), showing low dark cytotoxicity of **TPAM-2** NPs toward HeLa cells. However, the viability of HeLa cells was only 5% in the presence of **TPAM-2** NPs (20 μg mL^{-1}) under white light irradiation for 30 min. Dead cell imaging was performed to further assess the PDT effect of **TPAM-2** NPs (Fig. 6c). Propidium iodide (PI) was used to stain dead HeLa cells. HeLa cells incubated in the absence of **TPAM-2** NPs under white light irradiation for 30 min gave almost no red fluorescence, indicating that light irradiation itself did not damage the cells. However, HeLa cells incubated in the presence of **TPAM-2** NPs at 20 μg mL^{-1} under white light irradiation for 30 min exhibited bright red fluorescence. The above results reveal the good PDT performance of **TPAM-2** NPs for HeLa cells.

4. Conclusion

In summary, we have reported a rational molecular design strategy to enhance NIR AIE of a photosensitizer for AIE imaging-guided PDT via rotor effect. The core of the developed strategy is to introduce molecular rotors into the photosensitizer to enhance the competition of AIE over TICT while not significantly to impair the ability for $^1O_2$ production. The rotor effect not only improves the AIE effect through decreasing intermolecular interactions in the aggregate state, but also disturbs the TICT effect through balancing D–π–A strength. Based on the developed strategy, we have designed and prepared a novel photosensitizer **TPAM-2** with strong NIR luminescence and good capability for $^1O_2$ production. We have also employed amphiphilic polymer DSPE-PEG_{2000} to encapsulate **TPAM-2** for the preparation of hydrophilic and biocompatible **TPAM-2** NPs. The fabricated **TPAM-2** NPs have exhibited good potential for AIE imaging-guided PDT for HeLa cells. This work provides a promising way to design ideal AIE imaging-guided photosensitizers for cancer theranostics.

Credit author statement

Dong-Hui Wang, Methodology, Compound synthesis, Data curation, Writing – original draft. Li-Jian Chen, Formal analysis. Xu Zhao, Formal analysis. Xiu-Ping Yan, Conceptualization, Funding acquisition, Resources, Supervision, Writing-Reviewing and Editing.

Declaration of competing interest

We declare no competing financial interest.

Acknowledgements

The authors are thankful for the financial support from National Natural Science Foundation of China (No. 21934002, 21804056, and 21804057), Postgraduate Research & Practice Innovation Program of Jiangsu Province (No. KYCX20_1775), and Natural Science Foundation of Jiangsu Province, China (No. BK20180581 and BK20180584), National First-class Discipline Program of Food Science and Technology (No. JUFSTR20180301), and Collaborative Innovation Center of Food Safety and Quality Control in Jiangsu Province.

Appendix A. Supplementary data

Supplementary data to this article can be found online at https://doi.org/10.1016/j.talanta.2020.122046.

References

[1] H.I. Pass, Photodynamic therapy in oncology: mechanisms and clinical use, J. Natl. Cancer Inst. 85 (1993) 443–456.

[2] A.P. Castano, P. Mroz, M.R. Hamblin, Photodynamic therapy and anti-tumour immunity, Nat. Rev. Canc. 6 (2006) 535–545.

[3] P. Agostinis, K. Berg, K.A. Cengel, T.H. Foster, A.W. Girotti, S.O. Gollnick, S. M. Hahn, M.R. Hamblin, A. Juzeniene, D. Kessel, M. Korbelik, J. Moan, P. Mroz, D. Nowis, J. Piette, B.C. Wilson, J. Golab, Photodynamic therapy of cancer: an update, CA A Cancer J. Clin. 61 (2011) 250–281.

[4] K. Kostovic, Z. Pastar, R. Ceovic, Z. Bukvic Mokos, D. Stulhofer Buzina, A. Stanimirovic, Photodynamic therapy in dermatology: current treatments and implications, Coll. Antropol. 36 (2012) 1477–1481.

[5] Y. Hayata, H. Kato, C. Konaka, J. Ono, N. Takizawa, Hematoporphyrin derivative and laser photoradiation in the treatment of lung cancer, Chest 81 (1982) 269–277.

[6] U.O. Nseyo, J. DeHaven, T.J. Dougherty, W.R. Potter, D.L. Merrill, S.L. Lundahl, D. L. Lamm, Photodynamic therapy (PDT) in the treatment of patients with resistant superficial bladder cancer: a long term experience, J. Clin. Laser Med. Surg. 16 (1998) 61–68.

[7] R. Bonnett, Photosensitizers of the porphyrin and phthalocyanine series for photodynamic therapy, Chem. Soc. Rev. 24 (1995) 19–33.

[8] A.B. Ormond, H.S. Freeman, Dye sensitizers for photodynamic therapy, Materials 6 (2013) 817–840.

[9] H. Abrahamse, M.R. Hamblin, New photosensitizers for photodynamic therapy, Biochem. J. 473 (2016) 347–364.

[10] F. Hu, S. Xu, B. Liu, Photosensitizers with aggregation-induced emission: materials and biomedical applications, Adv. Mater. 30 (2018) 1801350.

[11] X. Li, S. Lee, J. Yoon, Supramolecular photosensitizers rejuvenate photodynamic therapy, Chem. Soc. Rev. 47 (2018) 1174–1188.

[12] N.D. Cosgrove, A.M. Al-Osaimi, H.K. Sanoff, M.M. Morris, P.W. Read, D.G. Cox, J. A. Mann, C.K. Argo, C.L. Berg, S.J. Pelletier, D.G. Maluf, A.Y. Wang, Photodynamic therapy provides local control of cholangiocarcinoma in patients awaiting liver transplantation, Am. J. Transplant. 14 (2014) 466–471.

[13] J.P. Celli, B.Q. Spring, I. Rizvi, C.L. Evans, K.S. Samkoe, S. Verma, B.W. Pogue, T. Hasan, Imaging and photodynamic therapy: mechanisms, monitoring, and optimization, Chem. Rev. 110 (2010) 2795–2838.

[14] A. Kamkaew, S.H. Lim, H.B. Lee, L.V. Kiew, L.Y. Chung, K. Burgess, BODIPY dyes in photodynamic therapy, Chem. Soc. Rev. 42 (2013) 77–88.

[15] M. Ethirajan, Y. Chen, P. Joshi, R.K. Pandey, The role of porphyrin chemistry in tumor imaging and photodynamic therapy, Chem. Soc. Rev. 40 (2011) 340–362.

[16] J. Luo, Z. Xie, J.W.Y. Lam, L. Cheng, B.Z. Tang, H. Chen, C. Qiu, H.S. Kwok, X. Zhan, Y. Liu, D. Zhu, Aggregation-induced emission of 1-methyl-1,2,3,4,5-pentaphenylsilole, Chem. Commun. (2001) 1740–1741.

[17] J.B. Xiong, H.T. Feng, J.P. Sun, W.Z. Xie, D. Yang, M. Liu, Y.S. Zheng, The fixed propeller-like conformation of tetraphenylethylene that reveals aggregation-induced emission effect, chiral recognition, and enhanced chiroptical property, J. Am. Chem. Soc. 138 (2016) 11469–11472.

[18] X.H. Wang, N. Song, W. Hou, C.Y. Wang, Y. Wang, J. Tang, Y.W. Yang, Efficient aggregation-induced emission manipulated by polymer host materials, Adv. Mater. 31 (2019) 1903962.

[19] M. Zhang, M.L. Saha, M. Wang, Z. Zhou, B. Song, C. Lu, X. Yan, X. Li, F. Huang, S. Yin, P.J. Stang, Multicomponent platinum(II) cages with tunable emission and amino acid sensing, J. Am. Chem. Soc. 139 (2017) 5067–5074.

[20] Y. Li, Z. Li, Y. Wang, A. Compaan, T. Ren, W.-J. Dong, Increasing the power output of a CdTe solar cell via luminescent down shifting molecules with intramolecular charge transfer and aggregation-induced emission characteristics, Energy Environ. Sci. 6 (2013) 2907–2911.

[21] J. Huang, N. Sun, Y. Dong, R. Tang, P. Lu, P. Cai, Q. Li, D. Ma, J. Qin, Z. Li, Similar or totally different: the control of conjugation degree through minor structural modifications, and deep-blue aggregation-induced emission luminogens for non-doped OLEDs, Adv. Funct. Mater. 23 (2013) 2329–2337.

[22] W. Qin, K. Li, G. Feng, M. Li, Z. Yang, B. Liu, B.Z. Tang, Bright and photostable organic fluorescent dots with aggregation-induced emission characteristics for noninvasive long-term cell imaging, Adv. Funct. Mater. 24 (2014) 635–643.

[23] G. Cheng, H. Wang, C. Zhang, Y. Hao, T. Wang, Y. Zhang, Y. Tian, J. Chang, Multifunctional nano-photosensitizer: a carrier-free aggregation-induced emission nanoparticle with efficient photosensitization and pH-responsibility, Chem. Eng. J. 390 (2020) 124447.

[24] X. Li, M. Jiang, J.W.Y. Lam, B.Z. Tang, J.Y. Qu, Mitochondrial imaging with combined fluorescence and stimulated Raman scattering microscopy using a probe of the aggregation-induced emission characteristic, J. Am. Chem. Soc. 139 (2017) 17022–17030.

[25] W. Fu, C. Yan, Z. Guo, J. Zhang, H. Zhang, H. Tian, W.H. Zhu, Rational design of near-infrared aggregation-induced-emission-active probes: in situ mapping of amyloid-β plaques with ultrasensitivity and high-fidelity, J. Am. Chem. Soc. 141 (2019) 3171–3177.

[26] X. Ni, X. Zhang, X. Duan, H.-L. Zheng, X.-S. Xue, D. Ding, Near-infrared afterglow luminescent aggregation-induced emission dots with ultrahigh tumor-to-liver signal ratio for promoted image-guided cancer surgery, Nano Lett. 19 (2019) 318–330.

[27] G. Yu, T.R. Cook, Y. Li, X. Yan, D. Wu, L. Shao, J. Shen, G. Tang, F. Huang, X. Chen, P.J. Stang, Tetraphenylethene-based highly emissive metallacage as a component of theranostic supramolecular nanoparticles, Proc. Natl. Acad. Sci. U.S.A. 113 (2016) 13720–13725.

[28] S. Liu, X. Zhou, H. Zhang, H. Ou, J.W.Y. Lam, Y. Liu, L. Shi, D. Ding, B.Z. Tang, Molecular motion in aggregates: manipulating TICT for boosting photothermal theranostics, J. Am. Chem. Soc. 141 (2019) 5359–5368.

[29] G. Feng, W. Wu, S. Xu, B. Liu, Far red/near-infrared AIE dots for image-guided photodynamic cancer cell ablation, ACS Appl. Mater. Interfaces 8 (2016) 21193–21200.

[30] F. Hu, Y. Huang, G. Zhang, R. Zhao, H. Yang, D. Zhang, Targeted bioimaging and photodynamic therapy of cancer cells with an activatable red fluorescent bioprobe, Anal. Chem. 86 (2014) 7987–7995.

[31] W. Wu, D. Mao, F. Hu, S. Xu, C. Chen, C.J. Zhang, X. Cheng, Y. Yuan, D. Ding, D. Kong, B. Liu, A highly efficient and photostable photosensitizer with near-infrared aggregation-induced emission for image-guided photodynamic anticancer therapy, Adv. Mater. 29 (2017) 1700548.

[32] Y. Chen, W. Ai, X. Guo, Y. Li, Y. Ma, L. Chen, H. Zhang, T. Wang, X. Zhang, Z. Wang, Mitochondria-targeted polydopamine nanocomposite with aie photosensitizer for image-guided photodynamic and photothermal tumor ablation, Small 15 (2019) 1902352.

[33] J. Mei, N.L. Leung, R.T. Kwok, J.W. Lam, B.Z. Tang, Aggregation-induced emission: together we shine, united we soar!, Chem. Rev. 115 (2015) 11718–11940.

[34] Y. Wu, W. Zhu, Organic sensitizers from D-π-A to D-A-π-A: effect of the internal electron-withdrawing units on molecular absorption, energy levels and photovoltaic performances, Chem. Soc. Rev. 42 (2013) 2039–2058.

[35] Z.R. Grabowski, K. Rotkiewicz, W. Rettig, Structural changes accompanying intramolecular electron transfer: focus on twisted intramolecular charge-transfer states and structures, Chem. Rev. 103 (2003) 3899–4032.

[36] W. Rettig, Charge separation in excited states of decoupled systems—TICT compounds and implications regarding the development of new laser dyes and the primary process of vision and photosynthesis, Angew. Chem. Int. Ed. 25 (1986) 971–988.

[37] S.Y. Lee, T. Yasuda, Y.S. Yang, Q. Zhang, C. Adachi, Luminous butterflies: efficient exciton harvesting by benzophenone derivatives for full-color delayed fluorescence OLEDs, Angew. Chem. Int. Ed. 53 (2014) 6402–6406.

[38] S.M.A. Fateminia, L. Kacenauskaite, C.J. Zhang, S. Ma, Kenry, P.N. Manghnani, J. Chen, S. Xu, F. Hu, B. Xu, B.W. Laursen, B. Liu, Simultaneous increase in brightness and singlet oxygen generation of an organic photosensitizer by nanocrystallization, Small 14 (2018) 1803325.

[39] J. Liu, C. Chen, S. Ji, Q. Liu, D. Ding, D. Zhao, B. Liu, Long wavelength excitable near-infrared fluorescent nanoparticles with aggregation-induced emission characteristics for image-guided tumor resection, Chem. Sci. 8 (2017) 2782–2789.

[40] S. Sasaki, G.P.C. Drummen, G.-i. Konishi, Recent advances in twisted intramolecular charge transfer (TICT) fluorescence and related phenomena in materials chemistry, J. Mater. Chem. C 4 (2016) 2731–2743.

[41] S.S. Lucky, K.C. Soo, Y. Zhang, Nanoparticles in photodynamic therapy, Chem. Rev. 115 (2015) 1990–2042.

[42] K. Li, B. Liu, Polymer-encapsulated organic nanoparticles for fluorescence and photoacoustic imaging, Chem. Soc. Rev. 43 (2014) 6570–6597.

[43] H. Xu, L. Cheng, C. Wang, X. Ma, Y. Li, Z. Liu, Polymer encapsulated upconversion nanoparticle/iron oxide nanocomposites for multimodal imaging and magnetic targeted drug delivery, Biomaterials 32 (2011) 9364–9373.

[44] S. Sivakumar, V. Bansal, C. Cortez, S.-F. Chong, A.N. Zelikin, F. Caruso, Degradable, surfactant-free, monodisperse polymer-encapsulated emulsions as anticancer drug carriers, Adv. Mater. 21 (2009) 1820–1824.